High-Gain Nonlinear Active Disturbance Rejection Control Strategy for Traction Permanent Magnet Motor Drives

Yin Bai, Guoqiang Zhang, *Senior Member, IEEE*, Qiwei Wang, *Member, IEEE*, Dawei Ding, *Member, IEEE*, Binxing Li, Gaolin Wang, *Senior Member, IEEE*, and Dianguo Xu, *Fellow, IEEE*

***Abstract*—In order to improve the performance of the traction permanent magnet motor drives without weight transducer for direct-drive elevator applications during starting operation, this article proposes a novel control method based on the high-gain nonlinear active disturbance rejection control (HNLADRC) strategy. First, the limitation of linear and nonlinear error decay function of active disturbance rejection control (ADRC) method is analyzed, which is not suitable for the complex situation at starting operation of the traction motor. A high-gain nonlinear error decay function based ADRC method is proposed, which can achieve better performance in the starting operation of the traction motor. Both the high-gain extended state observer (HNLESO) and the high-gain nonlinear error feedback law (HNLEFL) are constructed by the high-gain error decay function to improve the compensation accuracy of the starting torque and the dynamics of the speed loop. By analyzing the error decay performance of the HNLESO and the HNLEFL, it is proved that the HNLADRC method has a faster error decay rate. Experimental results show that the proposed method can obtain a shorter rollback distance and faster response capability.**

***Index Terms*—Error feedback law, extended state observer, high-gain nonlinear active disturbance rejection, starting control strategy, traction permanent magnet motor.**

I. Introduction

THE traction permanent magnet motor has replaced the traditional geared traction machine as the mainstream traction machine due to the high efficiency, simple structure, and high-power density [1]–[5]. In the starting operation of the elevator, the rollback problem of the car is the main factor affecting the comfort of the passengers. The traditional method is to install the weight transducer at the bottom of the car which measures and compensates the starting torque to suppress the rollback of the car. However, the installation of the weight transducer is complicated, and the inaccurate compensation may occur when the sensor fails, affecting the performance of the elevator. Thus, the weight-transducerless control method has become the development trend in the elevator industry. Due to the low bandwidth of the speed loop and poor stiffness of the traction motor system, the PI controller is difficult to effectively suppress the rollback phenomenon of the elevator car in the weight-transducerless control method [6].

At present, some research works have been carried out to investigate the starting performance of the traction motor, which is mainly divided into two categories, the direct calculation method and the controller method. The direct calculation method mainly establishes the mechanic model of the traction motor, through which the starting torque can be calculated and compensated. In [7], the research pointed out that the force model of the traction motor is the nonlinear load with time variation. On this basis, the starting torque was compensated in the control system in [8]. The direct calculation method requires the high precision of modeling, which is still at the approximate stage and cannot compensate the starting torque accurately. In [9], the dichotomy method was used to approximate the starting torque, which can further improve the calculation accuracy of the direct calculation method. However, the calculation accuracy of the direct calculation method is still low for the starting torque, which limits the situation where the starting torque needs to be compensated accurately.

The controller method is to replace the traditional control algorithm in the system with the advanced control algorithm to improve the response ability and reduce the steady-state error, such as fuzzy control algorithm [10], [11] and model predictive control (MPC) algorithm [12]–[15]. By making fuzzy rules [10] to self-tune the parameters, the fuzzy controller can adaptively adjust the bandwidth under different system disturbances [11]. The MPC algorithm can effectively improve the response speed due to the good control performance for nonlinear systems [14], [15]. Predictive control can also be combined with other advanced control algorithms, such as sliding mode control [16] and adaptive control [18], to further increase the system stiffness. In [17], a delay compensation algorithm based on MPC was proposed to reduce the influence of digital delay on system

Manuscript received 26 January 2022; revised 7 April 2022; accepted 30 May 2022. Date of publication 7 June 2022; date of current version 26 July 2022. This work was supported in part by the Research Fund for the National Natural Science Foundation of China under Grants 52125701 and 52177034 and in part by the Fundamental Research Funds for the Central Universities under Grant FRFCU5710092020. Recommended for publication by Associate Editor S. Williamson. *(Corresponding author: Guoqiang Zhang.)*

The authors are with the School of Electrical Engineering and Automation, Harbin Institute of Technology, Harbin 150001, China (e-mail: baiyinhit@163.com; zhgq@hit.edu.cn; wqw0543@163.com; dingdawei@hit.edu.cn; li_binxing@163.com; wgl818@hit.edu.cn; xudiang@hit.edu.cn).

Color versions of one or more figures in this article are available at https://doi.org/10.1109/TPEL.2022.3180348.

Digital Object Identifier 10.1109/TPEL.2022.3180348

response. Generally speaking, the controller method has strict requirements for the design of internal parameters. The inaccurate parameters may lead to unstable operation of the system, so the parameter design is complicated.

Another controller method is the active disturbance rejection control (ADRC) method. Since the complex load during the starting operation can be regarded as system disturbance, the ADRC method can be adopted. The ADRC can effectively suppress the total disturbance by observing the system disturbance through the extended state observer (ESO) and feeding forward compensation to the control signal [24]–[29]. In [24], the stability of the ADRC method was analyzed in detail, and the selection rule of the parameters was given. On this basis, a cascade ESO was proposed in [25], where the disturbance was observed again through two observers to reduce the observation error. In view of the noise in the input signal, a noise suppression method in the ESO was proposed in [26] to reduce the influence of high-frequency noise while improving the observation bandwidth. The core of the ADRC method is the error decay function. The linear function is widely used as the simplest form of function. The error decay effect of the nonlinear function is better than the linear function at certain conditions. However, the decay rate of the nonlinear error function is smaller than that of the linear error function when the system disturbance is large. For the complex situation at starting operation of the traction motor, one error decay function cannot satisfy the requirement of fast error decay. Thus, the high-gain processing of nonlinear function can realize fast convergence of errors.

The main contribution of this article is to propose a high-gain nonlinear active disturbance rejection control strategy for traction permanent magnet motor drive. On the basis of analyzing the performance of traditional linear and nonlinear error decay functions, a high-gain nonlinear error decay function is proposed. This function can achieve a large gain and obtain a better decay effect than the traditional linear and nonlinear error decay functions. The high-gain nonlinear error decay function is applied to the ESO to realize a fast and accurate observation of system disturbance. The high-gain nonlinear control law is applied to the nonlinear error feedback to form the high-gain nonlinear error feedback control law, which can reduce the rollback distance and time when the traction motor starts. The effectiveness of the proposed scheme is verified on the 11.7 kW traction permanent magnet motor experimental platform.

II. Limitation of Traditional ADRC for Traction Motor Drives

A. Model of Traction Motor Drive Adopting ADRC

Fig. 1 shows the structure of the traditional ADRC, which can be divided into linear active disturbance rejection controller (LADRC) and nonlinear active disturbance rejection controller (NLADRC) according to different error decay functions.

The mechanic equation of the traction motor is shown as

$$\begin{cases} \dot{\theta}_e = \omega_e \\ \dot{\omega}_e = \frac{1}{J}(T_e - T_L) - \frac{B\omega_e}{J} \\ \dot{T}_L = 0 \end{cases} \tag{1}$$

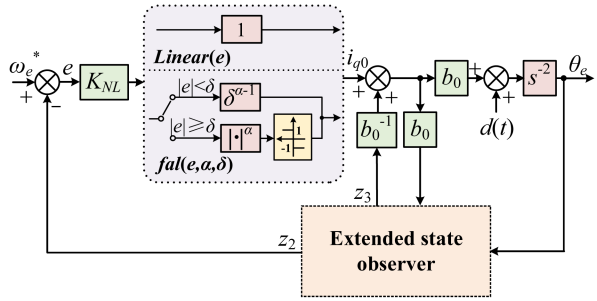

Fig. 1. Structure diagram of traditional ADRC.

where θ_e is the position of the traction motor, ω_e is the mechanic speed, T_e is the output torque, T_L is the load torque, B is the friction coefficient, and J is the moment of inertia. For the field-oriented control system, the q-axis current reference $i_q{}^*$ can be regarded as the control quality under the mode of $i_d = 0$.

Suppose $d(t) = (T_e\text{-}T_L)/J\text{-}B\omega_e/J\text{-}b_0 i_q{}^*$, where $d(t)$ is the total disturbance of the system. Through $m(t)$ and (1), the state function of the system can be expressed as

$$\begin{cases} \dot{\theta}_e = \omega_e \\ \dot{\omega}_e = m(t) + b_0 i_q^* \\ \dot{m}(t) = h \end{cases} \tag{2}$$

where h is the change rate of the start torque. When the motor is in the zero-servo stage, $\omega_e = 0$, and there is no electromagnetic torque. At this time, the total disturbance can be equated to the start load torque T_L. The figure shows the main process of load torque applied to the elevator traction machine, which is divided into three main steps as follows: Step I, the brake holds the brake wheel; step II, the brake is gradually released; step III, the brake is completely released. The function of the equivalent load torque of the traction motor is shown as

$$T_{\mathrm{L}} = \begin{cases} 0, F_{\mathrm{b}} + F_{\mu} > (M_{\mathrm{c}} - M_{\mathrm{w}})g \\ [(M_{\mathrm{c}} - M_{\mathrm{w}})g - (F_{\mathrm{b}} + F_{\mu})]R, \ F_{\mathrm{b}} \\ +F_{\mu} \le (M_{\mathrm{c}} - M_{\mathrm{w}})g \end{cases} \tag{3}$$

where F_{b} is the frictional force by the brake, $F\mu$ is the frictional force by other factors in the dynamic process of the system, and R is the radius of the traction wheel.

Fig. 2 shows the increasing progress of start load torque. It can be seen from the figure that the starting torque is loaded in a continuous process and therefore the differential h is consistent. The third-order ESO is established based on (1)

$$\begin{cases} e_1 = z_1 - \theta_e \\ \dot{z}_1 = z_2 - l_1\xi_1(e_1) \\ \dot{z}_2 = z_3 + b_0 i_q^* - l_2\xi_2(e_1) \\ \dot{z}_3 = -l_3\xi_3(e_1) \end{cases} \tag{4}$$

where e_1 is the error between the estimated position and θ_{e}, d_0 is the torque constant, z_1, z_2, and z_3 are the estimated values of θ_e, ω_e, and $m(t)$, respectively, and $\xi(e)$ is the error decay function of the ESO. $\xi(e)$ is the core of the ESO, deciding the decay way of the estimated error.

The error decay functions of the traditional linear extended state observer (LESO) and nonlinear extended state observer

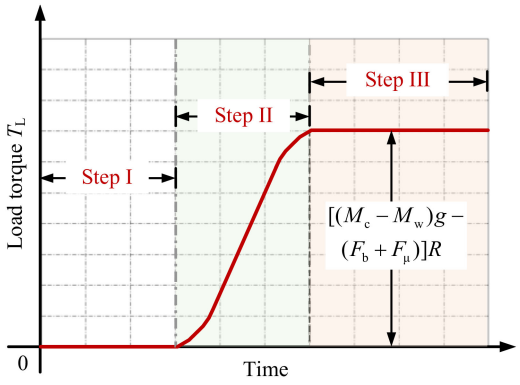

Fig. 2. Increasing progress of start load torque.

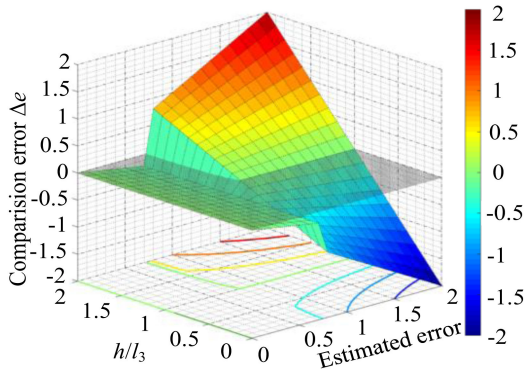

Fig. 3. Relationship of Δe, h/l_3, and estimated error.

(NLESO) are shown as

$$\xi_L(e) = e \tag{5}$$

$$\xi_{NL}(e) = \text{fal}(e,\alpha,\delta) = \begin{cases} \frac{e}{\delta^{1-\alpha}}, |e| < \delta \\ |e|^{\alpha}\text{sign}(e), |e| \geq \delta \end{cases} \tag{6}$$

where $\xi_L(e)$ is the error decay function of LESO, $\xi_{NL}(e)$ is the error decay function of NLESO. *fal* function is used as the nonlinear error decay function, where $0<\alpha<1$ and $0<\delta<1$.

After compensating the starting torque using ESO, the P controller is commonly used as the speed controller due to the integral effect of ESO. However, the response time of the speed loop is slow because of the removal of the integral part, making the rollback distance significantly larger than before. After removing the integral part, the speed loop system needs to be processed to further reduce the rollback distance. The disturbance immunity of the system is analyzed setting the control quantity as $i_q^* = i_{q0}$. Suppose the output of the speed loop as the traditional nonlinear function

$$i_{q0} = K_{NL} fal(e,\alpha,\delta) = \begin{cases} K_{\text{NL}}\frac{e}{\delta^{1-\alpha}}, |e| < \delta \\ K_{\text{NL}}|e|^{\alpha}\text{sign}(e), |e| \geq \delta \end{cases} \tag{7}$$

where K_{NL} is the proportional coefficient of the nonlinear part. The feedback system is changed into the linear feedback when $\alpha = 1$. The speed state function is shown as

$$\begin{aligned} \dot{\omega} &= d(t) + b_0 i_{q0} \\ &= d(t) + b_0 K_{\text{NL}}\text{fal}(e,\alpha,\delta). \end{aligned} \tag{8}$$

Due to $e = -\omega_e$ at zero-speed starting operation, the speed error can be calculated by (8)

$$\dot{e} = d(t) - b_0 K_{\text{NL}}\text{fal}(e,\alpha,\delta). \tag{9}$$

B. Analysis of Limitation of Traditional ADRC

Define $e_2 = z_2 - \omega_e$, $e_3 = z_3 - m(t)$, the error state function can be shown as

$$\begin{cases} \dot{e}_1 = e_2 - l_1\xi_1(e_1) \\ \dot{e}_2 = e_3 - l_2\xi_2(e_1) \\ \dot{e}_3 = h - l_3\xi_3(e_1) \end{cases}. \tag{10}$$

When the system reaches the steady state after compensation at startup, satisfy $\dot{e}_1 = \dot{e}_2 = \dot{e}_3 = 0$. The relationship of the estimated errors between LESO and NLESO is shown as

$$\begin{cases} e_{N1,2,3\infty} = \delta^{1-\alpha} e_{L1,2,3\infty}, |e_{N1\infty}| \leq \delta \\ e_{N1,2,3\infty} = \left(\frac{|h|}{l_3}\right)^{\frac{1}{\alpha}-1} e_{L1,2,3\infty}, |e_{N1\infty}| > \delta \end{cases}. \tag{11}$$

Define $\Delta e = e_{\text{N1,2,3}\infty} - e_{\text{L1,2,3}\infty}$. The relationship of Δe, h/l_3, and the estimated error is shown in Fig. 3.

According to (11) and Fig. 3, when $|e| \leq \delta$, $\delta^{1-\alpha} < 1$ and $e_{\text{N1,2,3}\infty} < e_{\text{L1,2,3}\infty}$ because α and δ are less than 1. Thus, the position estimated error of NLESO is less than that of LESO. When $|e| > \delta$, the convergence of NLESO is related to h/l_3. When $h > l_3$, $e_{\text{N1,2,3}\infty} > e_{\text{L1,2,3}\infty}$, showing that NLESO has the higher steady-state estimated accuracy of the starting torque at the small change rate h. When the large change rate of the starting torque is added, $h = l_3(|e| = 1)$ is bounded, pointing out that LESO has higher estimated accuracy at $h > l_3$ ($|e| > 1$), and the NLESO has higher estimated accuracy at $h < l_3$ ($|e| < 1$).

The limitations of the traditional error feedback control law are analyzed. The differential equation is shown in the following equation:

$$\frac{1}{1+\alpha}\frac{d|e|^{1+\alpha}}{dt} = |e|^{\alpha}\text{sign}(e)\frac{de}{dt}. \tag{12}$$

Multiply both sides of (12) by $\frac{1}{1+\alpha}\frac{d|e|^{1+\alpha}}{dt}$

$$\frac{1}{1+\alpha}\frac{d|e|^{1+\alpha}}{dt} = \begin{cases} -b_0 K_{\text{NL}}\delta^{\alpha-1}\left(e - \frac{m(t)}{2b_0 K_{\text{NL}}}\right)^2 + \frac{(m(t))^2}{4b_0 K_{\text{NL}}}, |e| < \delta \\ -b_0 K_{\text{NL}}\left(|e|^{\alpha}\text{sign}(e) - \frac{m(t)}{2b_0 K_{\text{NL}}}\right)^2 + \frac{(m(t))^2}{4b_0 K_{\text{NL}}} |e| \geq \delta \end{cases}. \tag{13}$$

Suppose the amplitude of the starting torque is m_0. According to (13), the condition should be met to satisfy $d|e|^{1+\alpha}/dt$

$$\begin{cases} e > \frac{m_0}{\delta^{1-\alpha} b_0 K_{\text{NL}}}, |e| < \delta \\ |e|^{\alpha} > \frac{m_0}{b_0 K_{\text{NL}}}, |e| \geq \delta \end{cases}. \tag{14}$$

That is, the error of the speed loop eventually enters the interval

$$\begin{cases} \left[-\frac{m_0}{\delta^{1-\alpha} b_0 K_{\text{NL}}}, \frac{m_0}{\delta^{1-\alpha} b_0 K_{\text{NL}}}\right], |e| < \delta \\ \left[-\left(\frac{m_0}{b_0 K_{\text{NL}}}\right)^{\frac{1}{\alpha}}, \left(\frac{m_0}{b_0 K_{\text{NL}}}\right)^{\frac{1}{\alpha}}\right], |e| \geq \delta \end{cases}.$$

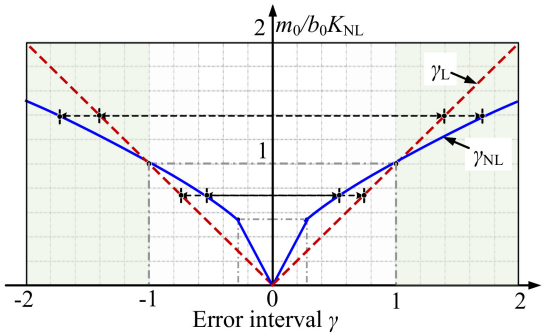

Fig. 4. Relationship among m_0/b_0K_{NL}, γ_L, and γ_{NL}.

When $\alpha = 1$, the system changes into the linear system, resulting in the error of the speed loop system eventually enter the interval ($-m_0/b_0K_{NL}$, m_0/b_0K_{NL}). Assume γ_L and γ_{NL} are the upper bounds of the error decay range of the linear and *fal* functions, respectively. The relations between m_0/b_0K_{NL}, γ_L, and γ_{NL} can be obtained

$$\frac{m_0}{b_0K_{NL}} = \gamma_L = \begin{cases} \frac{\gamma_{NL}}{\delta^{1-\alpha}}, |\gamma_{NL}| < \delta \\ (\gamma_{NL})^{\alpha}\text{sign}(\gamma_{NL}), |\gamma_{NL}| \geq \delta \end{cases}. \quad (15)$$

Fig. 4 shows the relationship among m_0/b_0K_{NL}, γ_L, and γ_{NL}. It can be seen that the length of the error interval of the linear and nonlinear error decay functions is related to the value of m_0/b_0K_{NL}. When $(m_0/b_0K_{NL})<1$, $\gamma_L<\gamma_{NL}$, the decay interval of nonlinear error function is smaller. When the starting torque is large, $(m_0/b_0K_{NL})>1$,$\gamma_L>\gamma_{NL}$, the linear error function decay interval is smaller.

It can be concluded that the limitation of the traditional ADRC mainly depends on the choice of error decay function. Both the linear and nonlinear error decay functions have advantages and disadvantages under different load conditions, but they cannot achieve an ideal effect under complex load conditions when the motor starts. Therefore, it is necessary to improve the error decay function, so that the observation error and control error can converge quickly, effectively improve the observation accuracy of the torque and the stiffness of the control system.

III. Proposed High-Gain Nonlinear ADRC Strategy

The field-oriented control scheme of the direct drive permanent magnet traction machine for starting is shown in Fig. 5(a), in which the proposed HNLADRC is used. The HNLADRC mainly includes two parts, the high-gain nonlinear extended state observer (HNLESO) and the high-gain nonlinear error feedback law (HNLEFL). The whole control algorithm is completed in a digital signal processor chip. Fig. 5(b) is the structure diagram of the proposed traction machine starting control strategy.

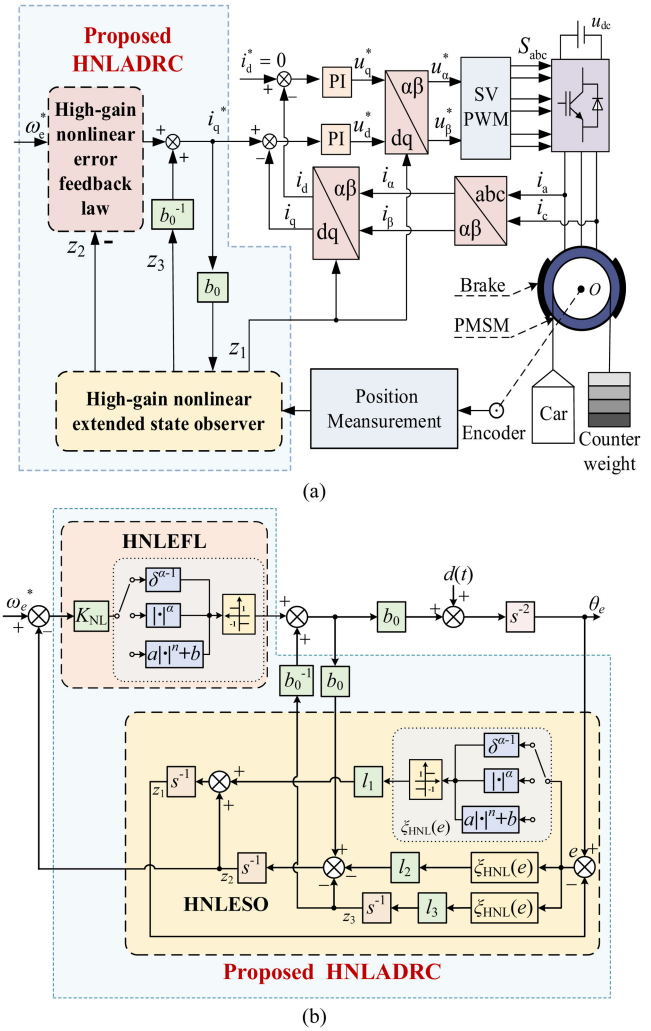

Fig. 5. Block diagram of HNLADRC. (a)Field-oriented control diagram. (b)Structure of HNLADRC.

A. High-Gain Nonlinear Extended State Observer

Take the derivative of the *fal* function

$$\frac{dfal(e_1,\alpha,\delta)}{de_1} = \begin{cases} \frac{1}{\delta^{1-\alpha}}, |e_1| \leq \delta \\ \alpha|e_1|^{\alpha-1}\text{sign}(e_1), |e_1| \leq \delta \end{cases}. \quad (16)$$

When the error is in the nonlinear part, the point at which the derivative equals 1 is ($\alpha^{1/(1-\alpha)}$, $\alpha^{\alpha/(1-\alpha)}$). When the derivative is greater than 1, the higher order function is considered to obtain larger gain than the linear function and the *fal* function. The high-gain *fal* function is shown as follows:

$$nfal(e,\alpha,\delta) = \begin{cases} \frac{e}{\delta^{1-\alpha}}, |e| < \delta \\ |e|^{\alpha}\text{sign}(e), \delta \leq |e| \leq \alpha^{\frac{1}{1-\alpha}} \\ (a|e|^{n}+b)\text{sign}(e), |e| > \alpha^{\frac{1}{1-\alpha}} \end{cases}. \quad (17)$$

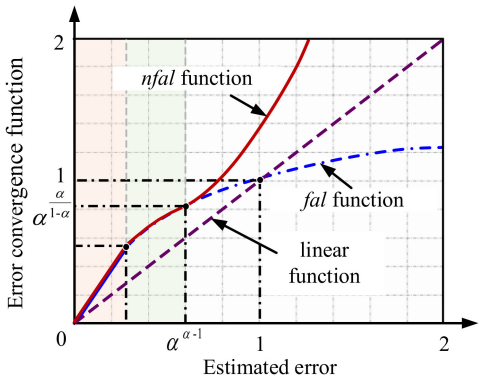

Fig. 6. Function image of linear, *fal*, and *nfal* function.

By substituting $(\alpha^{1/(1-\alpha)}, \alpha^{\alpha/(1-\alpha)})$ and the derivative into (17), the coefficient can be obtained as

$$\begin{cases} a = \frac{1}{n}\alpha^{\frac{n-1}{\alpha-1}} \\ b = \alpha^{\frac{\alpha}{1-\alpha}} - \frac{1}{n}\alpha^{\frac{1}{1-\alpha}} \end{cases}. \tag{18}$$

Fig. 6 shows the function image of the linear function, the *fal* function, and the *nfal* function. Since the three functions are all odd functions, the function properties of the first quadrant are analyzed here. It can be seen that the *nfal* function has the same structure as the *fal* function in $(0, \alpha^{1/(1-\alpha)})$, while the *nfal* function adopts a higher-order function for error decay. According to the structure shown in Fig. 4(b), the ESO using the *nfal* function can be expressed as

$$\begin{cases} e_1 = z_1 - \theta_e \\ \dot{z}_1 = z_2 - l_1 nfal(e_1, \alpha, \delta) \\ \dot{z}_2 = z_3 + bi_q^* - l_2 nfal(e_1, \alpha, \delta) \\ \dot{z}_3 = -l_3 nfal(e_1, \alpha, \delta) \end{cases}. \tag{19}$$

When the traction motor adopts the ESO based on the *nfal* function, the steady-state error of the system can be obtained. The error is the same as that of *fal* function when $|e|<\alpha^{1/(1-\alpha)}$. The error function in $|e|>\alpha^{1/(1-\alpha)}$ is shown as

$$\begin{cases} \mathrm{e_{HN1\infty}} = \left[\mathrm{n}\frac{\mathrm{h}}{\mathrm{k_3}} - \left(\mathrm{n}\alpha^{\frac{\alpha}{1-\alpha}} - \alpha^{\frac{1}{1-\alpha}}\right)\right]\alpha^{\frac{\mathrm{n}-1}{\mathrm{n}(1-\alpha)}} \\ \mathrm{e_{HN2\infty}} = \mathrm{l_1 e_{HN1\infty}} \\ \mathrm{e_{HN3\infty}} = \mathrm{l_2 e_{HN1\infty}} \end{cases}. \tag{20}$$

The steady-state errors of the linear function, the *fal* function, and the *nfal* function are compared when $|e|>\alpha^{1/(1-\alpha)}$. When $|e|<1$, the *fal* function has a smaller steady-state error. When $|e|>1$, the linear function has a smaller steady-state error. Hence, the *nfal* function is compared with *fal* function when $|e|<1$, and compared with linear function when $|e|>1$. Define

$$\begin{cases} \Delta e_1 = \mathrm{e_{HN1\infty}} - \mathrm{e_{N1\infty}}, |\mathrm{e_{HN1\infty}}| < \alpha^{\frac{1}{1-\alpha}}, |\mathrm{e_{N1\infty}}| < \alpha^{\frac{1}{1-\alpha}} \\ \Delta e_2 = \mathrm{e_{HN1\infty}} - \mathrm{e_{L1\infty}}, |\mathrm{e_{HN1\infty}}| > \alpha^{\frac{1}{1-\alpha}}, |\mathrm{e_{N1\infty}}| > \alpha^{\frac{1}{1-\alpha}} \end{cases}. \tag{21}$$

Fig. 7 shows the relationship of Δe_1 and Δe_2 about function order n and estimated error e, where the shaded surface is the error when Δe_1 and Δe_2 equals 0. As can be seen, the regions of

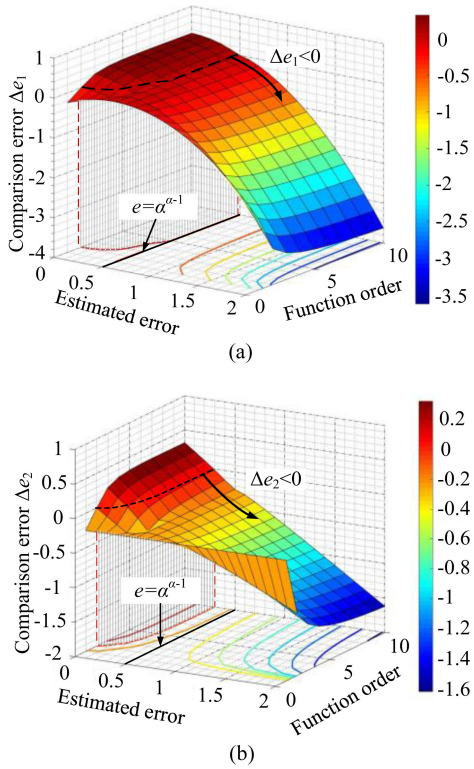

Fig. 7. Relationship of comparison error, estimated error e and function order n. (a) Δe_1. (b) Δe_2.

$|e|>\alpha^{1/1-\alpha}$ are all distributed in $\Delta e_1<0$ and $\Delta e_2<0$. Therefore, it can be seen that the HNLESO has a small steady-state convergence error, and it can accurately observe the starting torque.

B. High-Gain Nonlinear Error Feedback Control Law

The structure of the HNLEFL is shown in Fig. 5(b), where the proposed *nfal* function is considered to deal with the nonlinear error feedback system. As seen from (17), the error of *nfal* function can be shown as follows when $|e|>\alpha^{1/(1-\alpha)}$

$$\frac{1}{n}\alpha^{\frac{n-1}{\alpha-1}}|e|^n + \alpha^{\frac{\alpha}{1-\alpha}} - \frac{1}{n}\alpha^{\frac{1}{1-\alpha}}. \tag{22}$$

Change the differential function to

$$\frac{\alpha^{\frac{n-1}{\alpha-1}}}{n(1+\alpha)}\frac{d|e|^{1+n}}{dt} = \frac{1}{n}\alpha^{\frac{n-1}{\alpha-1}}|e|^n \mathrm{sign}(e)\frac{de}{dt}. \tag{23}$$

It can be obtained from (23)

$$\begin{aligned} &\frac{\alpha^{\frac{n-1}{\alpha-1}}}{n(1+\alpha)}\frac{d|e|^{1+n}}{dt} = \\ &-b_0 K_{\mathrm{NL}}\left(\frac{1}{n}\alpha^{\frac{n-1}{\alpha-1}}|e|^n - \frac{1}{2}\left(\frac{m(t)}{b_0 K_{\mathrm{NL}}} - \alpha^{\frac{\alpha}{1-\alpha}} + \frac{1}{n}\alpha^{\frac{1}{1-\alpha}}\right)\right)^2 \\ &+ \frac{1}{4b_0 K_{\mathrm{NL}}}\left(\frac{m(t)}{b_0 K_{\mathrm{NL}}} - \alpha^{\frac{\alpha}{1-\alpha}} + \frac{1}{n}\alpha^{\frac{1}{1-\alpha}}\right)^2, |e| \geq \alpha^{\alpha-1}. \end{aligned} \tag{24}$$

If the left of (21) is less than 0, the condition to be satisfied is

$$|e|^n > \frac{n}{2}\alpha^{\frac{1-n}{\alpha-1}}\left(\frac{m_0}{b_0 K_{\mathrm{NL}}} - \alpha^{\frac{\alpha}{1-\alpha}} + \frac{1}{n}\alpha^{\frac{1}{1-\alpha}}\right). \tag{25}$$

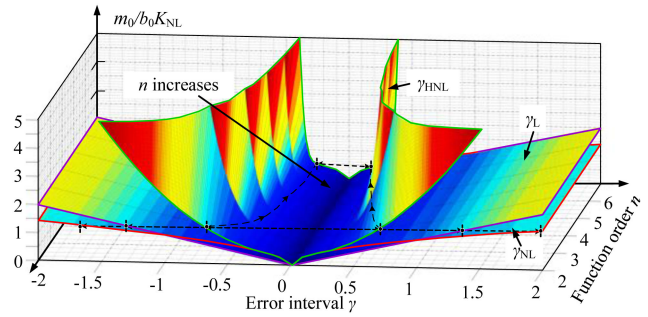

Fig. 8. Relationship among γ_L, γ_{NL}, and γ_{HNL}.

Therefore, the error of the speed loop system eventually falls into the interval

$$\left(-\frac{n}{2}\alpha^{\frac{1-n}{n(\alpha-1)}}\left(\frac{m_0}{b_0K_{NL}}-\alpha^{\frac{\alpha}{1-\alpha}}+\frac{1}{n}\alpha^{\frac{1}{1-\alpha}}\right)^{\frac{1}{n}} \right. \left. \frac{n}{2}\alpha^{\frac{1-n}{n(\alpha-1)}}\left(\frac{m_0}{b_0K_{NL}}-\alpha^{\frac{\alpha}{1-\alpha}}+\frac{1}{n}\alpha^{\frac{1}{1-\alpha}}\right)^{\frac{1}{n}} \right).$$

Assume γ_{HNL} is the upper bound of error decay of the high-gain nonlinear error decay function. The relationship among γ_L, γ_{NL}, and γ_{HNL} is shown in Fig. 8. It can be seen that the error of the *nfal* function is smaller than that of the linear and *fal* function at the same m_0/b_0K_{NL} value. And the error decay interval gradually decreases with the increase of the function order n. Therefore, after using the HNLEFL, the traction motor can get a smaller rollback distance at startup.

C. Error Decay Characteristics of HNLADRC

Define the error gain function

$$\lambda(e)=\frac{nfal(e)}{e}=\begin{cases}\frac{1}{\delta^{1-\alpha}}, |e|<\delta\\ |e|^{\alpha-1}\text{sign}(e), \delta\le|e|\le\alpha^{\frac{1}{1-\alpha}}\\ (a|e|^{n-1}+\frac{b}{e})\text{sign}(e), |e|>\alpha^{\frac{1}{1-\alpha}}\end{cases}. \tag{26}$$

The HNLESO can be expressed as the variable gain ESO by the error gain function

$$\begin{cases}e_1=z_1-\theta_e\\ \dot{z}_1=z_2-l_1\lambda_{n1}e_1\\ \dot{z}_2=z_3+bi_q^*-l_2\lambda_{n2}e_1\\ \dot{z}_3=-l_3\lambda_{n3}e_1\end{cases}. \tag{27}$$

Assume the system reaches the steady state, $h=0$. Then the transfer function of the estimator can be obtained as follows:

$$\begin{cases}Z_1(s)=\frac{(l_1\lambda_{n1}s^2+l_2\lambda_{n2}s+l_3\lambda_{n3})\Theta(s)}{s^3+l_1\lambda_{n1}s^2+l_2\lambda_{n2}s+l_3\lambda_{n3}}+\frac{bsI(s)}{s^3+l_1\lambda_{n1}s^2+l_2\lambda_{n2}s+l_3\lambda_{n3}}\\ Z_2(s)=\frac{(l_2\lambda_{n2}s^2+l_3\lambda_{n3}s)\Theta(s)}{s^3+l_1\lambda_{n1}s^2+l_2\lambda_{n2}s+l_3\lambda_{n3}}+\frac{b(s^2+l_1\lambda_{n1}s)I(s)}{s^3+l_1\lambda_{n1}s^2+l_2\lambda_{n2}s+l_3\lambda_{n3}}\\ Z_3(s)=\frac{l_3\lambda_{n3}s^2\Theta(s)}{s^3+l_1\lambda_{n1}s^2+l_2\lambda_{n2}s+l_3\lambda_{n3}}-\frac{bl_3\lambda_{n3}I(s)}{s^3+l_1\lambda_{n1}s^2+l_2\lambda_{n2}s+l_3\lambda_{n3}}\end{cases} \tag{28}$$

where $Z_1(s)$, $Z_2(s)$, and $Z_3(s)$ are the Laplace transforms of z_1, z_2, and z_3, respectively. According to (25) and the error function, the transfer functions of the three errors are as (27), where $E_1(s)$, $E_2(s)$, and $E_3(s)$ are the Laplace transforms of e_1, e_2, and e_3, respectively, $\Theta(s)$ is the Laplace transform of θ_e, and $I(s)$ is the Laplace transform of $i_q{}^*$. Considering the steady-state convergence error of the third-order ESO, both the input and the controlled object are step signals with amplitude K are given as (28) in order to observe the response of the system

$$\begin{cases}E_1(s)=\frac{-s^3\Theta(s)+bsI(s)}{s^3+l_1\lambda_{n1}s^2+l_2\lambda_{n2}s+l_3\lambda_{n3}}\\ E_2(s)=\frac{-s^3(s+l_1\lambda_{n1})\Theta(s)+b(s^2+l_1\lambda_{n1}s)I(s)}{s^3+l_1\lambda_{n1}s^2+l_2\lambda_{n2}s+l_3\lambda_{n3}}\\ E_3(s)=\frac{-s^3(l_1\lambda_{n1}s^2+l_2\lambda_{n2}s+l_3\lambda_{n3})\Theta(s)}{s^3+l_1\lambda_{n1}s^2+l_2\lambda_{n2}s+l_3\lambda_{n3}}+\frac{b(s^3+l_1\lambda_{n1}s^2+l_2\lambda_{n2}s)I(s)}{s^3+l_1\lambda_{n1}s^2+l_2\lambda_{n2}s+l_3\lambda_{n3}}\end{cases} \tag{29}$$

$$\begin{cases}sE_1(s)=\frac{-Ks^3\Theta(s)+KbsI(s)}{s^3+l_1\lambda_{n1}s^2+l_2\lambda_{n2}s+l_3\lambda_{n3}}\\ sE_2(s)=\frac{-Ks^3(s+l_1\lambda_{n1})\Theta(s)+Kb(s^2+l_1\lambda_{n1}s)I(s)}{s^3+l_1\lambda_{n1}s^2+l_2\lambda_{n2}s+l_3\lambda_{n3}}\\ sE_3(s)=\frac{-Ks^3(l_1\lambda_{n1}s^2+l_2\lambda_{n2}s+l_3\lambda_{n3})\Theta(s)}{s^3+l_1\lambda_{n1}s^2+l_2\lambda_{n2}s+l_3\lambda_{n3}}+\frac{Kb(s^3+l_1\lambda_{n1}s^2+l_2\lambda_{n2}s)I(s)}{s^3+l_1\lambda_{n1}s^2+l_2\lambda_{n2}s+l_3\lambda_{n3}}\end{cases} \tag{30}$$

It can be seen from (27) that the transfer function of each error system has the same characteristic function

$$R(s)=s^3+l_1\lambda_{n1}s^2+l_2\lambda_{n2}s+l_3\lambda_{n3} \tag{31}$$

To simplify the calculation, set $\lambda_{n1}=\lambda_{n2}=\lambda_{n3}=\lambda$. The roots of the characteristic function s_1 and $s_{2,3}$ can be shown as

$$\begin{cases}s_1=-\omega_0-\frac{1}{3}\left(\sqrt[3]{y_1}+\sqrt[3]{y_2}\right)\\ s_{2,3}=\frac{1}{3}\left(-3\omega_0+\frac{1}{2}\left(\sqrt[3]{y_1}+\sqrt[3]{y_2}\right)\pm\frac{\sqrt{3}}{2}(\sqrt[3]{y_1}-\sqrt[3]{y_2})i\right)\end{cases} \tag{32}$$

where $y_1=27\omega_0^3(1-\lambda)(1+\sqrt{\lambda}), y_2=27\omega_0^3(1-\lambda)(1-\sqrt{\lambda})$, and ω_0 is the bandwidth of the ESO. The bandwidth of the ESO is determined by the shortest distance between the roots of the characteristic function and the imaginary axis. Thus, the bandwidth of the ESO can be characterized by

$$d=\min(|d_1|,|d_2|) \tag{33}$$

where d is the distance between the roots of the characteristic function and the imaginary axis, and d_1 and d_2 are the distances of the poles which can be shown as

$$\begin{cases}d_1=s_1=-\omega_0\left[1+\sqrt[3]{1-\lambda}(\sqrt[3]{1+\sqrt{\lambda}}+\sqrt[3]{1-\sqrt{\lambda}})\right]\\ d_2=\text{Re}(s_{2,3})=\\ -\omega_0\left[1-\frac{1}{2}\sqrt[3]{1-\lambda}\left(\sqrt[3]{1+\sqrt{\lambda}}+\sqrt[3]{1-\sqrt{\lambda}}\right)\right]\end{cases}. \tag{34}$$

The limits of d_1 and d_2 can be calculated as

$$\begin{cases}\lim\limits_{\lambda\to+\infty}d_1=-\frac{1}{3}\omega_0\\ \lim\limits_{\lambda\to0}d_2=0\end{cases}. \tag{35}$$

Fig. 9 shows the relationship of the distance from roots to the imaginary axis d and the nonlinear gain λ. It can be concluded that there exists the largest bandwidth ω_0 when λ changes within $(0,+\infty)$. Set the gain is λ_0 at ω_0. When $\lambda>\lambda_0$ and $\lambda\to+\infty$, $d=|d_1|$ and tends to $\omega_0/3$, indicating that the bandwidth of ESO is no less than 1/3 of the configured poles. When $\lambda<\lambda_0$, and $\lambda\to0$, $d=|d_2|$ and tends to 0, indicating that the bandwidth is tend to 0. In practical applications, λ is bounded, so the bandwidth should be selected with respect to the actual situation. The objective is to minimize the bandwidth variation range when λ is varied.

According to (33) and (35), the parameters of the characteristic function is configured as $l_1=3\omega_0$, $l_2=3\omega_0{}^2/\lambda_0$, $l_3=$

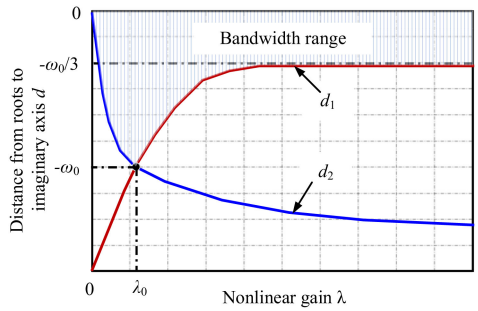

Fig. 9. Relationship of the distance from roots to imaginary axis d and nonlinear gain λ.

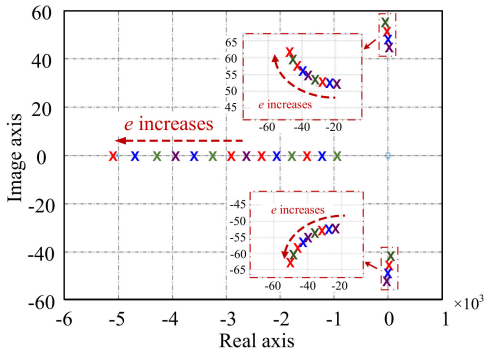

Fig. 10. Role figure of characteristic function.

$\omega_0{}^3/\lambda_0$. As can be seen from Fig. 10, when the error system changes with e, the poles of the closed-loop are always located in the left of the imaginary axis. Therefore, the system is stable for different errors. In addition, with the increase of error, the poles move away from the imaginary axis, which can accelerate the error convergence rate and achieve good error convergence performance.

The parameters of the nonlinear function are α and δ. Too small α may result in the high-frequency oscillation of observation, while the NLESO cannot play the advantages of fast error attenuation and strong anti-interference capability with large α. In general, α is taken as 0.5. δ determines the length of the linear interval. As known in Fig. 9 , too large linear interval δ brings about the failure of the nonlinear gain, while too small δ makes the observer more volatile. Generally, δ should be under the interval of [0.01, 0.1]. which is usually taken as $\delta = 0.1$.

The decay performance of the steady speed error is analyzed below. When the system disturbance is observed and compensated by the HNLESO, the output of the speed loop is

$$i_q^* = i_{q0} - \frac{z_2}{b_0}. \tag{36}$$

Due to the feedforward compensation effect of the ESO, the external disturbance of the system can be observed and suppressed. Therefore, the system can be regarded as a system without external disturbance, which can be simplified as $\dot{\omega} = i_{q0}$. During the zero-speed starting operation, e = -ω_e

$$\dot{e} = -K_{\mathrm{NL}}\psi(e) \tag{37}$$

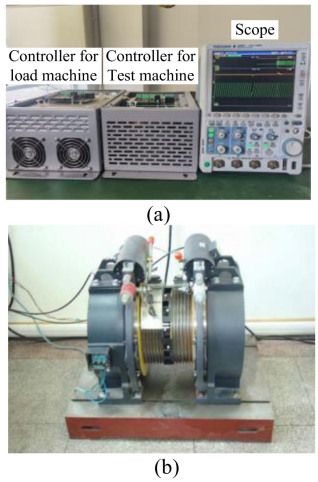

Fig. 11. Experimental platform of 11.7 kW gearless traction motor. (a) Traction motor drives. (b) Traction motor platform.

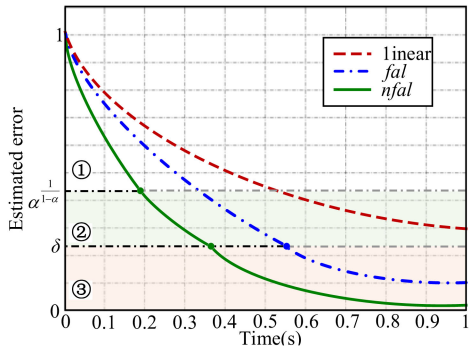

Fig. 12. Comparison of error decay speed of linear, *fal* and *nfal* function.

where $\psi(e)$ is the error decay function. It can be seen that K_{NL} is similar to the proportional part of the PI controller. Thus, K_{NL} can be adjusted according to the design method of the proportional part of the PI controller.

By substituting linear function, *fal* function, and *nfal* function into (31), the speed error can be obtained as follows:

$$e_L = e_0 e^{-K_{\mathrm{NL}}t} \tag{38}$$

$$e_{NL} = \begin{cases} e_0 e^{-\delta^{\alpha-1}K_{\mathrm{NL}}t}, |e| < \delta \\ \mathrm{sign}(e_0)\left(|e_0|^{1-\alpha} - (1-\alpha)K_{\mathrm{NL}}t\right)^{\frac{1}{1-\alpha}}, |e| \geq \delta \end{cases} \tag{39}$$

$$e_{HNL} = \begin{cases} e_0 e^{-\delta^{\alpha-1}K_{\mathrm{NL}}t}, |e| < \delta \\ \mathrm{sign}(e_0)\left(|e_0|^{1-\alpha} - (1-\alpha)K_{\mathrm{NL}}t\right)^{\frac{1}{1-\alpha}}, \delta \leq |e| < \alpha^{\frac{1}{1-\alpha}} \\ \dfrac{\mathrm{sign}(e_0)}{\left(\frac{1}{|e_0|^{\alpha-1}} + \alpha^{\frac{n-1}{\alpha-1}}(\alpha-1)K_{\mathrm{NL}}t\right)^{\frac{1}{\alpha-1}}}, |e| < \alpha^{\frac{1}{1-\alpha}} \end{cases} . \tag{40}$$

TABLE I
PMSM PARAMETERS

Parameter	Value	Parameter	Value
Rated Power	11.7 kW	Rated Torque	670N·m
Rated Speed	167 r/min	Resistance	0.23 Ω
Rated Frequency	33.4 Hz	Number of Pole Pairs	12
Rated Voltage	380 V	*d*-axis Inductance	15 mH
Rated Current	23 A	*q*-axis Inductance	15 mH

Fig. 12 shows the comparison of error decay speed of linear, *fal* and *nfal* functions. It can be seen that

1) The decay rate of linear function error satisfies the same exponential approaching law, which decays at the rate $e^{-K\mathrm{NL}t}$.
2) The decay rate of the *fal* function is divided into two parts. When $|e|<\delta$, the *fal* function decays at the rate of $e^{-\delta^{\alpha-1}K_{\mathrm{NL}}t}$; When $|e|>\delta$, the *fal* function decays at the rate of $((1\text{-}\alpha)K_{\mathrm{NL}}t)^{1/1\text{-}\alpha}$. It can be seen that the decay rate of the *fal* function is faster than the decay rate of the linear function.
3) The error decay rate of the *nfal* function is divided into three parts ①, ②, and ③. When $|e|\in(\alpha^{1/(1\text{-}\alpha)},1)$ the *nfal* function decays at the rate of $(\alpha^{(n\text{-}1)/(\alpha\text{-}1)}(1\text{-}\alpha)K_{\mathrm{NL}}t)^{1/(1\text{-}\alpha)}$. When $|e|<\alpha^{1/(1\text{-}\alpha)}$ the decay rate of *nfal* is the same as that of the *fal* function. It can be seen that after *nfal* function, the steady-state error amplitude and decay speed of the system are better than the linear function and the *fal* function. Therefore, the nonlinear error feedback control law using the *nfal* function can effectively reduce the rollback distance and rollback time.

IV. EXPERIMENTAL RESULTS

The proposed method was verified on the platform of the traction permanent magnet motor drives as shown in Fig. 11. The parameters of the traction motor are shown in Table I. The whole field-oriented control algorithm is executed with a low-cost ARM chip STM32F103VB in the gearless traction motor drive platform. The position sensor adopts ERN-1387 SIN/COS encoder whose resolution is 2048 P/R. The switching frequency of inverter is set as 6kHz. The periods of current and speed loops are set as 166.7 μs and 1 ms, respectively. In the experiments, set $\omega_0 = 50{*}2\pi$, $\alpha = 0.5$, $\delta = 0.1$, and $K_{\mathrm{NL}} = 5$.

Fig. 13 shows the error convergence waveform of the three functions under different disturbance rates at zero-speed starting operation. Fig. 13(a) shows the error convergence when $h/l_3 \approx 0.8$. The estimation error of LESO is 0.012π rad, and the convergence time is 1.36 s. The estimation error of the NLESO is 0.006π rad and the convergence time is 1.25 s. The estimation error is 0.003π and the convergence time is 1.21 s of the HNLESO. It can be seen that the convergence of the NLESO is better than that of the LESO. Fig. 13(b) shows the error convergence when $h/l_3 \approx 1.5$. The estimation error of LESO is 0.039π rad and the convergence time is 0.3 s. The estimation error of the NLESO is 0.044π rad, and the convergence time is 0.44 s. The estimation error is 0.019π rad and the convergence time is 0.18 s of the HNLESO. In this case, the convergence of LESO is better than

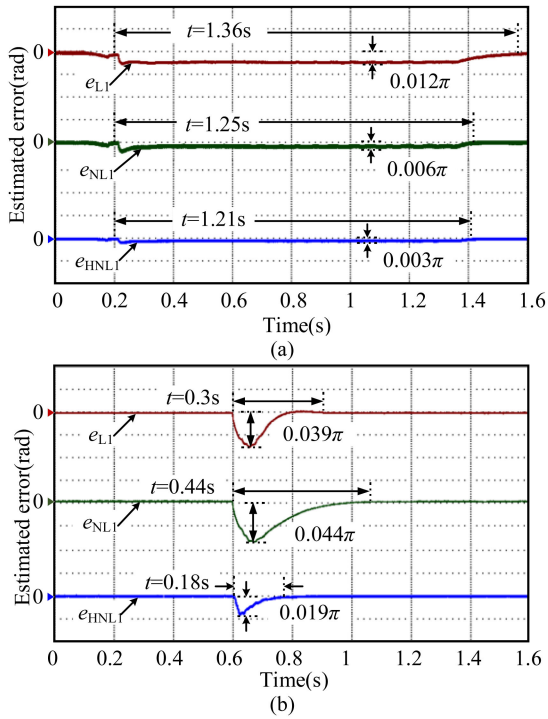

Fig. 13. Error convergence experimental waveforms under different disturbance rate. (a) $h/l_3 \approx 0.8$. (b) $h/l_3 \approx 1.5$.

that of NLESO. In both cases, the HNLESO is superior to LESO and NLESO in terms of convergence amplitude and convergence speed, which proves the effectiveness of the proposed method.

Fig. 14 shows the rollback distance comparison under 20% load, in which PI controller, the LADRC, the NLADRC and the HNLADRC are respectively adopted. As can be seen from Fig. 14, when PI controller is adopted, the rollback distance is the largest, reaching 1.35 mm, and the rollback time is 0.26 s. After compensating with the LADRC, the rollback distance is 0.78 mm and the rollback time is 0.35 s. Adopting the NLADRC can shorten the rollback distance to 0.42 mm, and the rollback time to 0.1 s. After adopting the HNLADRC, the rollback distance is shortened to 0.19 mm and the rollback time is shortened to 0.06 s.

Fig. 15 shows the rollback distance comparison under 60% load, in which PI controller, the LADRC, the NLADRC, and the HNLADRC are respectively adopted. As can be seen from Fig. 15, when PI controller is adopted, the rollback distance is the largest, reaching 4.68 mm, and the rollback time is 0.4 s. After adopting the LADRC, the rollback distance is shortened to 1.28 mm and the rollback time is 0.35 s. Adopting the NLADRC can shorten the rollback distance to 1.01 mm, and the rollback time to 0.16 s. After adopting the HNLADRC, the rollback distance is shortened to 0.69 mm and the rollback time is shortened to 0.12 s.

Fig. 16 shows the rollback distance comparison under 100% load, in which PI controller, the LADRC, the NLADRC, and the HNLADRC are respectively adopted. As can be seen from Fig. 16, when PI controller is adopted, the rollback distance is

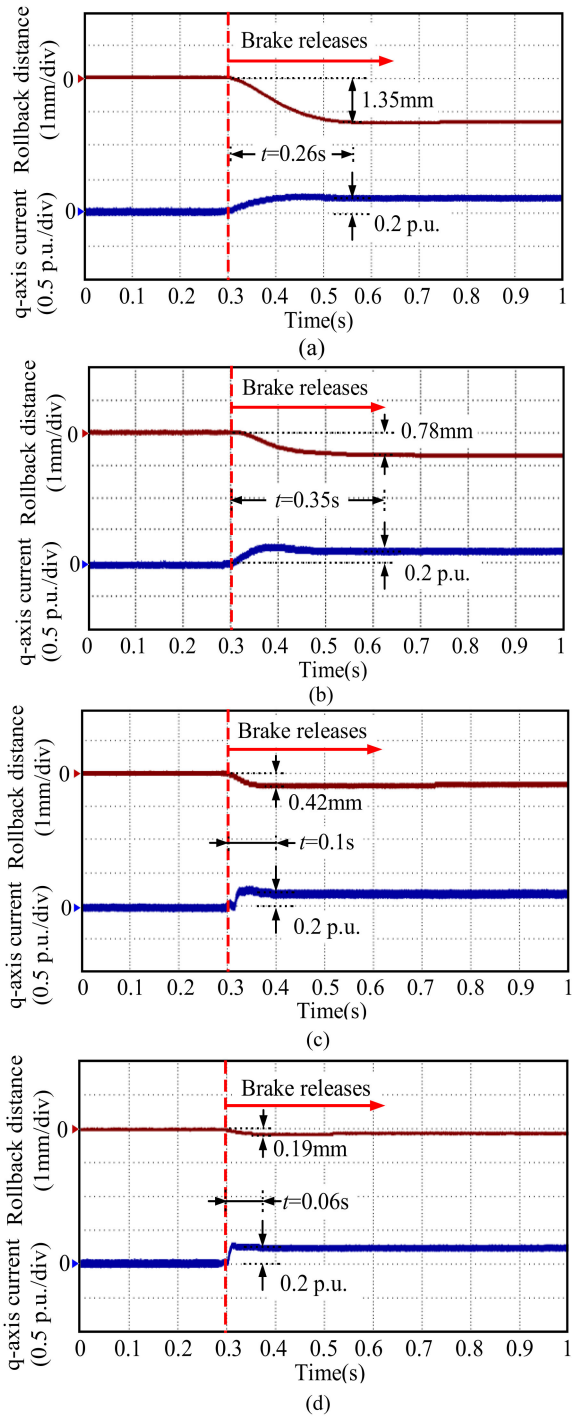

Fig. 14. Rollback distance and time under 20% of the rated load. (a) PI controller. (b) LADRC. (c) NLADRC. (d) HNLADRC.

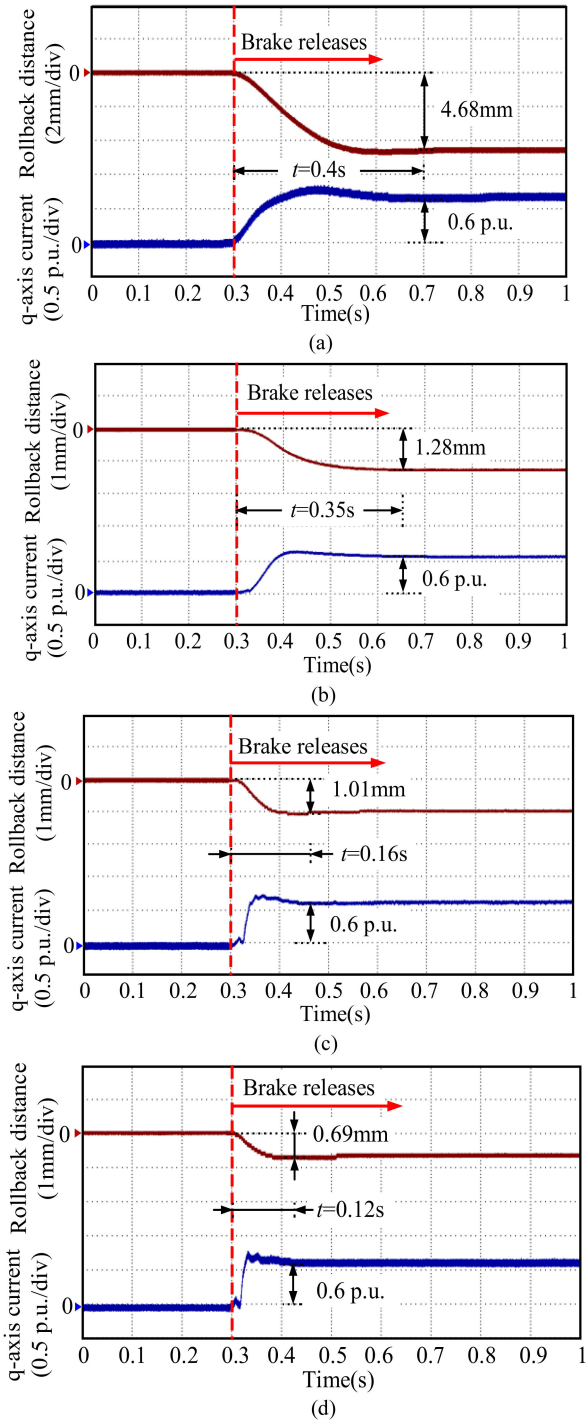

Fig. 15. Rollback distance and time under 60% of the rated load. (a) PI controller. (b) LADRC. (c) NLADRC. (d) HNLADRC.

the largest, reaching 7.84 mm, and the rollback time is 0.5 s. After compensating with the LADRC, the rollback distance is shortened to 1.53 mm and the rollback time is 0.36 s. Adopting the NLADRC can shorten the rollback distance to 1.62 mm and the rollback time to 0.17 s. After adopting the HNLADRC, the rollback distance is shortened to 1.05 mm and the rollback time is shortened to 0.10 s.

By applying different loads to the traction motor, it can be seen that the compensation effect of NLADRC is better than that of LADRC under light load. And the compensation effect of LADRC is better than that of NLADRC. The HNLADRC can obtain small rollback distance under different load conditions.

Fig. 17 shows the comparison of rollback distance and time of the four methods under different load conditions. Fig. 17(a)

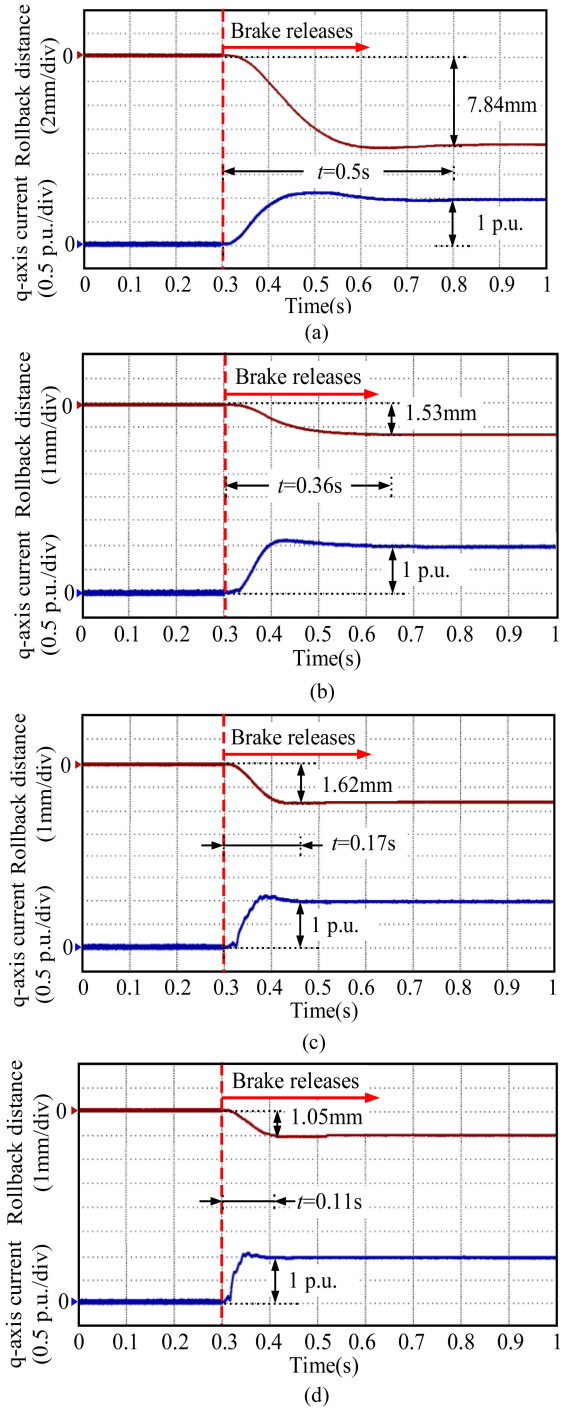

Fig. 16. Rollback distance and time under 100% of the rated load. (a) PI controller. (b) LADRC. (c) NLADRC. (d) HNLADRC.

shows the comparison of rollback distance. It can be seen that the rollback distance using PI controller is the largest. The LADRC has a smaller rollback distance at large load, while the NLADRC has a smaller rollback distance at small load. By the HNLADRC, the rollback distance can be effectively suppressed under full load condition. Fig. 17(b) shows the comparison of backsliding time of different methods. It can be seen from that when the load is small, the LADRC converges slowly and takes a long

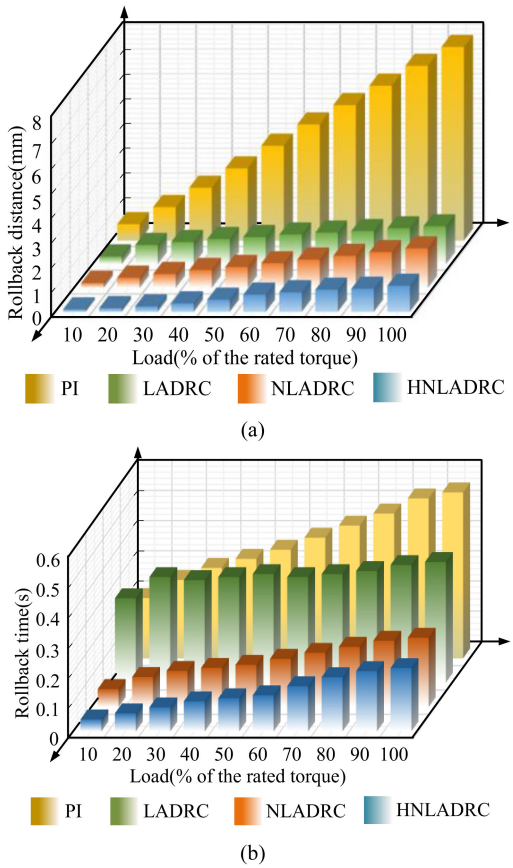

Fig. 17. Statistical diagrams of the rollback distance and rollback time. (a) Rollback distance. (b) Rollback time.

time to reach the steady state, resulting in a long rollback time. With the increase of load, the rollback time increases gradually. It can be seen from Fig. 15 that the rollback time decreases and the convergence speed accelerates after using the HNLADRC, which proves the effectiveness of the proposed method.

V. Conclusion

In this article, a high-gain nonlinear active disturbance rejection control strategy for traction permanent magnet motor drive is proposed. In order to improve the disturbance observation and compensation effect of the traditional ADRC, a high-gain nonlinear error decay function is proposed, which can achieve faster error decay. Compared with the traditional LESO and NLESO, this function can effectively improve the observation accuracy of the HNLESO. The HNLEFL is constructed by using the proposed high-gain error decay function. Compared with the traditional feedback control law, it can improve the speed error decay rate and reduce the steady-state error. Therefore, the proposed method can further reduce the rollback distance and time of the elevator under the complex load disturbance when the elevator starts. The experimental results show that the proposed can effectively reduce the rollback distance and time, and improve the starting performance of the traction motor.

REFERENCES

[1] G. Wang, J. Qi, J. Xu, X. Zhang, and D. Xu, "Antirollback control for gearless elevator traction machines adopting offset-free model predictive control strategy," *IEEE Trans. Ind. Electron.*, vol. 62, no. 10, pp. 6194–6203, Oct. 2015.

[2] G. Wang, M. Valla, and J. Solsona, "Position sensorless permanent magnet synchronous machine drives—A review," *IEEE Trans. Ind. Electron.*, vol. 67, no. 7, pp. 5830–5842, Jul. 2020.

[3] G. Wang, Y. Wang, J. Xu, N. Zhang, and D. Xu, "Weight-transducerless rollback mitigation adopting enhanced MPC with extended state observer for direct-drive elevators," *IEEE Trans. Power Electron.*, vol. 31, no. 6, pp. 4440–4451, Jun. 2016.

[4] M. S. Yoo, S. W. Park, H. J. Lee, and Y. D. Yoon, "Offline compensation method for current scaling gains in AC motor drive systems with three-phase current sensors," *IEEE Trans. Ind. Electron.*, vol. 68, no. 6, pp. 4760–4768, Jun. 2021.

[5] M. S. Yoo, S. W. Park, Y. Y. Choi, S. H. Han, and Y. D. Yoon, "Current-scaling gain compensation of motor drives under locked-rotor condition considering inequality of phase resistances," *IEEE Trans. Ind. Appl.*, vol. 56, no. 5, pp. 4915–4923, Sep./Oct. 2020.

[6] N. Jabbour and C. Mademlis, "Supercapacitor-based energy recovery system with improved power control and energy management for elevator applications," *IEEE Trans. Power Electron.*, vol. 32, no. 12, pp. 9389–9399, Dec. 2017.

[7] G. Wang, B. Wang, N. Zhao, and D. Xu, "Weight-transducerless control strategy based on active disturbance rejection theory for gearless elevator drives," *J. Power Electron.*, vol. 11, no. 2, pp. 289–299, 2016.

[8] A. Syafitri, M. K. I. Garniwa, R. Gunawan, and I. M. Ardita, "Variations on load and distance controller for modern elevator with fuzzy," in *Proc. 3rd Int. Conf. Inf. Technol., Comput., Elect. Eng.*, 2016, pp. 52–55.

[9] G. Wang, G. Zhang, R. Yang, and D. Xu, "Robust low-cost control scheme of direct-drive gearless traction machine for elevators without a weight transducer," *IEEE Trans. Ind. Appl.*, vol. 48, no. 3, pp. 996–1005, May/Jun. 2012.

[10] A. Syafitri, G. M. Iwa, R. Gunawan, and I. M. Ardita, "Fuzzy-PID simulation on current performance for modern elevator," in *Proc. 6th IEEE Int. Conf. Control Syst., Comput. Eng.*, 2016, pp. 403–406.

[11] G. Wang *et al.*, "Weight-transducerless starting torque compensation of gearless permanent-magnet traction machine for direct-drive elevators," *IEEE Trans. Ind. Electron.*, vol. 61, no. 9, pp. 4594–4604, Sep. 2014.

[12] J. Jung, V. Q. Leu, T. D. Do, E. Kim, and H. H. Choi, "Adaptive PID speed control design for permanent magnet synchronous motor drives," *IEEE Trans. Power Electron.*, vol. 30, no. 2, pp. 900–908, Feb. 2015.

[13] S. Kim and C. K. Ahn, "Offset-free proportional-type self-tuning speed controller for permanent magnet synchronous motors," *IEEE Trans. Ind. Electron.*, vol. 66, no. 9, pp. 7168–7176, Sep. 2019.

[14] T. Tarczewski and L. M. Grzesiak, "Constrained state feedback speed control of PMSM based on model predictive approach," *IEEE Trans. Ind. Electron.*, vol. 63, no. 6, pp. 3867–3875, Jun. 2016.

[15] Q. Wang *et al.*, "A low-complexity optimal switching time-modulated model-predictive control for PMSM with three-level NPC converter," *IEEE Trans. Transp. Electrific.*, vol. 6, no. 3, pp. 1188–1198, Sep. 2020.

[16] Z. Li, F. Wang, D. Ke, J. Li, and W. Zhang, "Robust continuous model predictive speed and current control for PMSM with adaptive integral sliding-mode approach," *IEEE Trans. Power Electron.*, vol. 36, no. 12, pp. 14398–14408, Dec. 2021.

[17] J. Gao, C. Gong, W. Li, and J. Liu, "Novel compensation strategy for calculation delay of finite control set model predictive current control in PMSM," *IEEE Trans. Ind. Electron.*, vol. 67, no. 7, pp. 5816–5819, Jul. 2020.

[18] S. Niu, Y. Luo, W. Fu, and X. Zhang, "Robust model predictive control for a three-phase PMSM motor with improved control precision," *IEEE Trans. Ind. Electron.*, vol. 68, no. 1, pp. 838–849, Jan. 2021.

[19] X. Zhang, B. Hou, and M. Yang, "Deadbeat predictive current control of permanent magnet synchronous motors with stator current and disturbance observer," *IEEE Trans. Power Electron.*, vol. 32, no. 5, pp. 3818–3834, May, 2017.

[20] M. Gu, Z. Wang, K. Yu, X. Wang, and M. Cheng, "Interleaved model predictive control for three-level neutral-point-clamped dual three-phase PMSM drives with low switching frequencies," *IEEE Trans. Power Electron.*, vol. 36, no. 10, pp. 11618–11630, Oct. 2021.

[21] M. S. R. Saeed, W. Song, B. Yu, and X. Wu, "Low-complexity deadbeat model predictive current control with duty ratio for five-phase PMSM drives," *IEEE Trans. Power Electron.*, vol. 35, no. 11, pp. 12085–12099, Nov. 2020.

[22] X. Gao, M. Abdelrahem, C. M. Hackl, Z. Zhang, and R. Kennel, "Direct predictive speed control with a sliding manifold term for PMSM drives," *IEEE Trans. Emerg. Sel. Topics Power Electron.*, vol. 8, no. 2, pp. 1258–1267, Jun. 2020.

[23] W. Tu, G. Luo, Z. Chen, C. Liu, and L. Cui, "FPGA implementation of predictive cascaded speed and current control of PMSM drives with two-time-scale optimization," *IEEE Trans. Ind. Inf.*, vol. 15, no. 9, pp. 5276–5288, Sep. 2019.

[24] A. M. Diab, S. Bozhko, M. Galea, and C. Gerada, "Stable and robust design of active disturbance-rejection current controller for permanent magnet machines in transportation systems," *IEEE Trans. Transp. Electrific.*, vol. 6, no. 4, pp. 1421–1433, Dec. 2020.

[25] G. Wang, R. Liu, N. Zhao, D. Ding, and D. Xu, "Enhanced linear ADRC strategy for HF pulse voltage signal injection-based sensorless IPMSM drives," *IEEE Trans. Power Electron.*, vol. 34, no. 1, pp. 514–525, Sep. 2019.

[26] Y. Zuo, J. Mei, C. Jiang, X. Yuan, S. Xie, and C. H. T. Lee, "Linear active disturbance rejection controllers for PMSM speed regulation system considering the speed filter," *IEEE Trans. Power Electron.*, vol. 36, no. 12, pp. 14579–14592, Dec. 2021.

[27] L. Qu, W. Qiao, and L. Qu, "Active-disturbance-rejection-based sliding-mode current control for permanent-magnet synchronous motors," *IEEE Trans. Power Electron.*, vol. 36, no. 1, pp. 751–760, Jan. 2021.

[28] C. Du, Z. Yin, Y. Zhang, J. Liu, X. Sun, and Y. Zhong, "Research on active disturbance rejection control of induction motors based on adaptive particle swarm optimization algorithm with dynamic inertia weight," *IEEE Trans. Power Electron.*, vol. 34, no. 3, pp. 2841–2855, Mar. 2019.

[29] B. Du, S. Wu, S. Han, and S. Cui, "Application of linear active disturbance rejection controller for sensorless control of internal permanent-magnet synchronous motor," *IEEE Trans. Ind. Electron.*, vol. 63, no. 5, pp. 3019–3027, May 2016.

Yin Bai received the B.S. and M.S degrees in electrical engineering, in 2017 and 2019, respectively, from Harbin Institute of Technology, Harbin, China, where he is currently working toward the Ph.D. degree in PMSM drives control.

His current research interests include advanced control of permanent magnet synchronous motor drives at low-speed operation.

Guoqiang Zhang (Senior Member, IEEE) received the B.S. degree in electrical engineering from Harbin Engineering University, Harbin, China, in 2011, and the M.S. and Ph.D. degrees in electrical engineering from Harbin Institute of Technology, Harbin, China, in 2013 and 2017, respectively.

Since 2017, he has been in the Department of Electrical Engineering, Harbin Institute of Technology, where he is currently an Associate Professor. His current research interests include control of electrical drives, and parameter identification technique, with main focus on sensorless field-oriented control of synchronous motor drives.

Dr. Zhang serves as an Associate Editor for *Journal of Power Electronics*.

Qiwei Wang (Member, IEEE) received the B.S., M.S., and Ph.D. degrees in electrical engineering from the Harbin Institute of Technology, Harbin, China, in 2015, 2017, and 2022, respectively, where he is currently working toward the Postdoc in power electronics and electrical drives in the School of Electrical Engineering and Automation.

His current research interests include parameter identification technique, and PMSM position sensorless control.

Dawei Ding (Member, IEEE) received the B.S. and M.S. degrees in electrical engineering from Hefei University of Technology, Hefei, China, in 2014 and 2017, respectively, and the Ph.D. degree in electrical engineering from Harbin Institute of Technology (HIT), Harbin, China, in 2021.

He is currently an Assistant Professor with the School of Electrical Engineering and Automation, HIT. From 2020 to 2021, he was a visiting Ph.D. in Technical University of Denmark. He has authored more than 10 journal papers in IEEE Transactions and held 9 authorized Chinese invention patents. His current research interests include advanced control of permanent magnet synchronous motor drives and electrolytic capacitorless ac motor drives.

Binxing Li received the B.S. degree in electrical engineering from the Harbin Institute of Technology, Weihai, China, in 2017. He is currently working toward the Ph.D. degree in power electronics and electrical drives at the Harbin Institute of Technology, Harbin, China.

His current research interests include permanent magnet synchronous motor drives, high efficiency ac–dc converter, and application of GaN power devices.

Gaolin Wang (Senior Member, IEEE) received the B.S., M.S., and Ph.D. degrees in electrical engineering from Harbin Institute of Technology, Harbin, China, in 2002, 2004, and 2008, respectively.

In 2009, he joined the Department of Electrical Engineering, Harbin Institute of Technology as a Lecturer, where he has been a Full Professor of Electrical Engineering since 2014. From 2009 to 2012, he was a Postdoctoral Fellow with Shanghai Step Electric Corporation, where he was involved in the traction machine control for direct-drive elevators. He has authored more than 60 technical papers published in IEEE Transactions. He is the holder of 30 Chinese patents. His current major research interests include permanent magnet synchronous motor drives, position sensorless control of ac motors, and digital control of power converters.

Dr. Wang serves as a Guest Associate Editor of IEEE TRANSACTIONS ON INDUSTRIAL ELECTRONICS, an Associate Editor of IEEE TRANSACTIONS ON TRANSPORTATION ELECTRIFICATION, IET ELECTRIC POWER APPLICATIONS, and *Journal of Power Electronics*.

Dianguo Xu (Fellow, IEEE) received the B.S. degree in control engineering from the Harbin Engineering University, Harbin, China, in 1982, and the M.S. and Ph.D. degrees in electrical engineering from the Harbin Institute of Technology (HIT), Harbin, China, in 1984 and 1989, respectively.

In 1984, he joined the Department of Electrical Engineering, HIT, as an Assistant Professor. Since 1994, he has been a Professor with the Department of Electrical Engineering, HIT. He was the Dean of the School of Electrical Engineering and Automation, HIT, from 2000 to 2010, and the Assistant President from 2010 to 2014. He is currently the Vice President of the HIT. He authored or coauthored more than 600 technical papers. His research interests include renewable energy generation technology, power quality mitigation, sensorless vector-controlled motor drives, high-performance PMSM servo system.

Dr. Xu is a Chairman of IEEE Harbin Section, Co-EIC of IEEE TRANSACTIONS ON POWER ELECTRONICS, Associate Editor of the IEEE TRANSACTIONS ON INDUSTRIAL ELECTRONICS, IEEE JOURNAL OF EMERGING AND SELECTED TOPICS IN POWER ELECTRONICS. He was the recipient of the 2018 IEEE IAS Outstanding Achievement Award.